Fuel 265 (2020) 116978

Contents lists available at ScienceDirect

Fuel

journal homepage: www.elsevier.com/locate/fuel

Full Length Article

3D measurements of hydrate surface area during hydrate dissociation in porous media using dynamic 3D imaging

Zaher A. Jarrar[a], Khalid A. Alshibli[a], Riyadh I. Al-Raoush[b,*], Jongwon Jung[c]

[a] Dept. of Civil & Env. Engineering, 325 John Tickle Building, University of Tennessee, Knoxville, TN 37996, USA
[b] Department of Civil and Architectural Engineering, Qatar University, P.O Box 2713, Doha, Qatar
[c] School of Civil Engineering, Chungbuk National University, Cheongju, Chungbuk 28644, South Korea

GRAPHICAL ABSTRACT

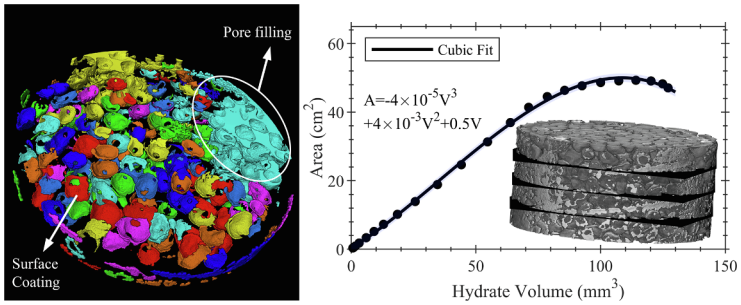

ARTICLE INFO

Keywords:
Gas hydrates
Computed tomography
3D imaging
Dissociation rate
Hydrate pore habit

ABSTRACT

A better understanding of the kinetics of hydrate dissociation is essential to reliably predict gas production potential from natural hydrate reservoirs. Most hydrate dissociation models assume hydrates to be a constant number of equal-sized spheres dissociating at a constant rate. This paper uses dynamic 3D synchrotron micro-computed tomography (SMT) imaging to study hydrate surface area evolution during Xenon hydrate dissociation. Hydrates are formed inside a high-pressure low-temperature cell filled with partially saturated ASTM 20-30 Ottawa sand. Hydrate dissociation is initiated through depressurization in the first experiment and through thermal stimulation in the second experiment. During dissociation, continuous full 3D SMT images were acquired where each scan took 45 s to complete. A combination of cementing, pore-filling, and surface coating pore habits were observed for the depressurization experiment and pore-filling for the thermal stimulation experiment. Surface coating hydrates dissociate faster than hydrates with pore-filling pore habit due to the higher specific area which allows for more surface for hydrates to dissociate it. Direct measurements of hydrate volume and hydrate surface area suggest that even with a combination of hydrate pore habits formed within the 3D porous media, estimation of hydrate surface area as a linear relation with (hydrate volume)$^{2/3}$ is best for hydrate saturation less than a threshold value depending on the dissociation method and driving force. (hydrate volume)^2 and (hydrate volume)^3 were found to better estimate hydrate interfacial area in comparison to (hydrate volume)$^{2/3}$ for the depressurization experiment and thermal stimulation experiment, respectively.

* Corresponding author.
E-mail addresses: zjarrar@vols.utk.edu (Z.A. Jarrar), alshibli@utk.edu (K.A. Alshibli), riyadh@qu.edu.qa (R.I. Al-Raoush), jjung@chungbuk.ac.kr (J. Jung).

https://doi.org/10.1016/j.fuel.2019.116978
Received 14 October 2019; Received in revised form 23 December 2019; Accepted 29 December 2019
Available online 07 January 2020

1. Introduction

Natural Methane (CH_4) gas hydrates availability and ongoing rise in demand for energy, motivated researchers to consider gas hydrates as a potential energy source. Gas hydrates refer to ice-like structures formed under certain pressure and temperature conditions where gas (guest molecules) is trapped within a crystal structure of water (host molecules) by van der Wall forces [1]. Different gas hydrate structures form depending on the molecular diameter of the guest molecules; primarily classified as structure I and structure II [2,3]. More than 95% of natural hydrates occur in marine environment where elevated pressure and low temperature conditions are satisfied [4,5], and approximately 99% of these hydrates are Methane hydrates [6,7]. Methane gas production from hydrate-bearing sediments requires hydrate dissociation in order to release Methane gas into sediments prior to gas production operations. Hydrate dissociation is a kinetic endothermic process that requires heat to break the bonds between guest and host molecules to produce water and gas. There are currently four main techniques to investigate hydrate dissociation; they are: thermal stimulation, depressurization, chemical injection and CH_4-CO_2 replacement [7–9].

Thermal stimulation and depressurization are applied by altering local pressure and temperature conditions of gas hydrate reservoirs,

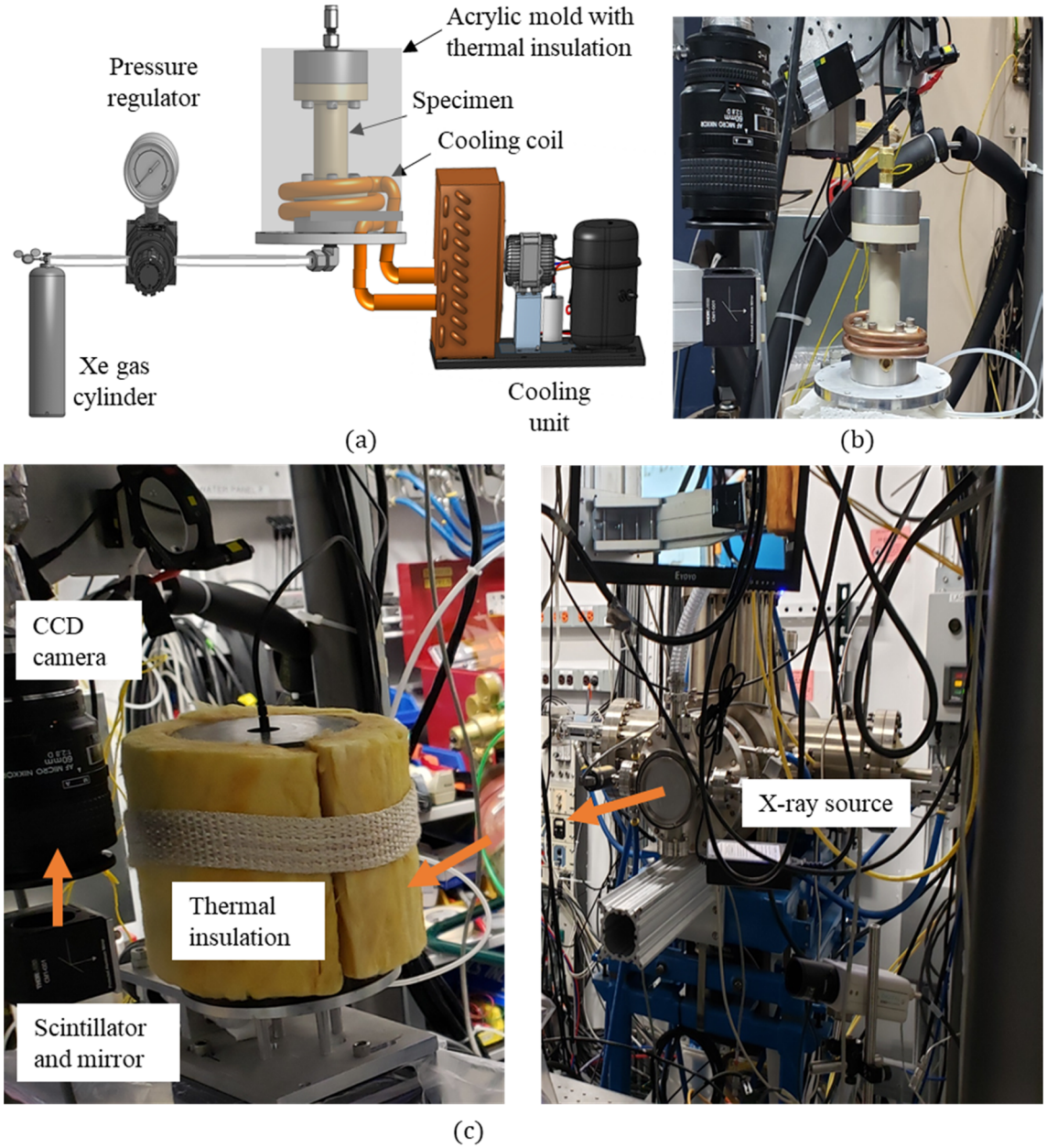

Fig. 1. (a) Schematic of the high-pressure low-temperature flow cell; (b) flow cell on stage without thermal insulation; and (c) experimental setup at Beamline 13D of the Advanced Photon Source, Argonne National Laboratory.

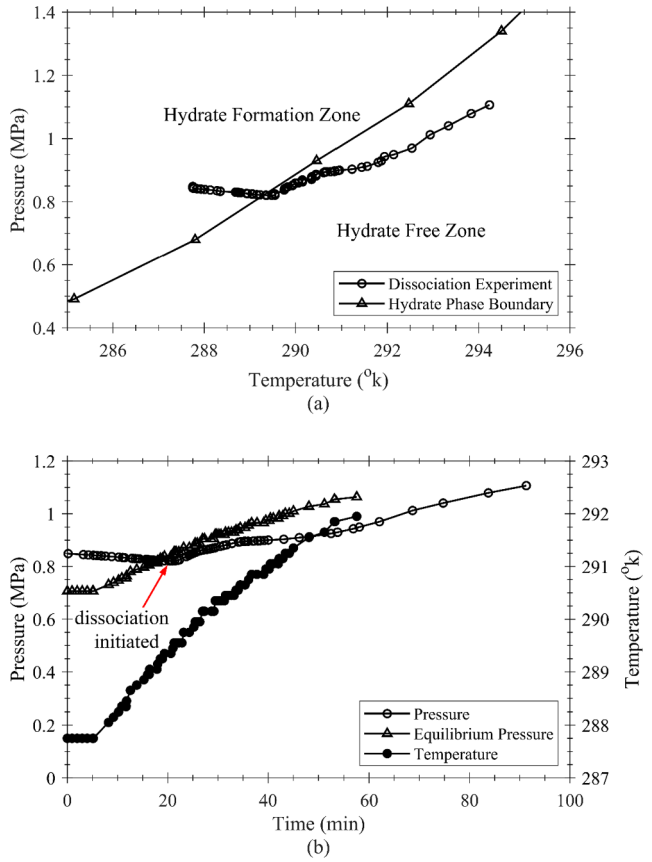

Fig. 2. (a) Hydrate phase boundary and experimental pressure–temperature measurments; and (b) change of temperature, pressure and hydrate equilibrium pressure during hydrate dissociation in the thermal stimulation experiment.

resulting in hydrate destabilization and dissociation to water and gas [10–13]. Chemical injection technique involves introducing a chemical to shift hydrate equilibrium curve for hydrates to dissociate at in-situ conditions [14,15], while CH_4-CO_2 replacement requires injecting CO_2 gas in hydrate reservoirs to replace CH_4 molecules in hydrate cages [16–19]. Among the four techniques, depressurization is considered the most economically feasible technique [20,21].

A better understanding of the kinetics of hydrate dissociation is essential to accurately predict gas production potential from natural hydrate reservoirs. Many theoretical [22,23], analytical [24,25], and numerical [26,27] dissociation kinetic models were developed by researchers since the 1980s to simulate hydrate dissociation process. Kim et al. [28] proposed what is considered as the most classical hydrate dissociation model until this date [29]. They studied Methane hydrate dissociation using a semi-batch stirred tank reactor, and proposed the hydrate dissociation rate to be:

$$-\frac{d_{n_H}}{d_t} = k_d A_S (f_e - f) \tag{1}$$

where $\frac{d_{n_H}}{d_t}$ is the molar hydrate dissociation rate (mol.s^{-1}), k_d is the hydrate dissociation rate constant (mol.m^{-2}.Pa^{-1}.s^{-1}), A_S is the surface area of hydrate (m^2), f_e is the fugacity of gas at hydrate equilibrium pressure and temperature conditions (Pa), and f is the fugacity of gas in the bulk gas phase (Pa). The hydrate dissociation rate constant can be described by an Arrhenius-type equation as:

$$k_d = k_d^0 e^{-\frac{\Delta E}{RT}} \tag{2}$$

where k_d^0 is the intrinsic dissociation rate constant (mol.m^{-2}.Pa^{-1}.s^{-1}), ΔE is the activation energy (J.mol^{-1}), R is the universal gas constant (8.314 J.mol^{-1}.k^{-1}), and T is the absolute temperature (k) [28,30]. Although the intrinsic dissociation rate constant is independent of pressure, temperature, and hydrate surface area, different studies reported different values of k_d^0 by orders of magnitude for batch reactors [28,30] and porous media [31,32]. This may be attributed to the fact that none of these studies measured the surface area of hydrates. They instead estimated the surface area based on hydrate particle size by either assuming they all have the same initial diameter [28], or by measuring hydrate particles sizes using particle size analyzer [30], or estimated the surface area as a linear combination of (hydrate saturation)$^{2/3}$ [31]. These estimates were based on the assumptions that hydrates are fixed number of spheres dissociating at a uniform rate, meaning that the surface area of hydrates can be estimated as a linear function of (hydrate volume)$^{2/3}$.

Recently, Chen, Espinoza [33] used microfocus x-ray radiography to study Xenon hydrate dissociation kinetics by first measuring the initial hydrate volume and surface area before dissociation based on a full reconstructed 3D image. They showed that hydrate surface area can be approximated as a linear function of (hydrate volume)$^{2/3}$. Then, they started hydrate dissociation by depressurization while capturing a total of 126 2D X-ray radiographs at a resolution of 49.79 μm /pixel and a time-resolution of 1 radiograph/second during the 40-minute dissociation experiment. Volume of hydrate was estimated based on assuming a linear relation between the change in hydrate volume and the change in x-ray numbers in the radiographs. The changes of those estimated volumes with time were used to calculate hydrate dissociation rates and reported a linear relationship between hydrate dissociation rate and (hydrate volume)$^{2/3}$.

This paper revisits the work of Chen, Espinoza [33]; however, it uses in-situ high-speed 3D tomography to study kinetics of Xenon hydrates dissociation and to directly measure volumes and surface areas of hydrates during dissociation. Hydrates were formed inside a special high-pressure low-temperature cell filled with partially saturated ASTM 20–30 Ottawa silica sand. Hydrate dissociation was triggered through depressurization and continuous full 3D SMT images were acquired during the dissociation. Direct measurements of hydrate volume and hydrate surface area were obtained from the images to test the validity hydrate surface area estimation commonly used in hydrate dissociation models. Additionally, effects of hydrate pore habit and specific surface on hydrate dissociation rate were investigated.

2. Materials and experimental setup

In this study, Methane gas was substituted by Xenon gas; an analog to Methane gas in previous studies, due to its high X-ray attenuation coefficients compared to Methane, which enhances phase contrast between hydrate and other phases in the reconstructed images [34–36].

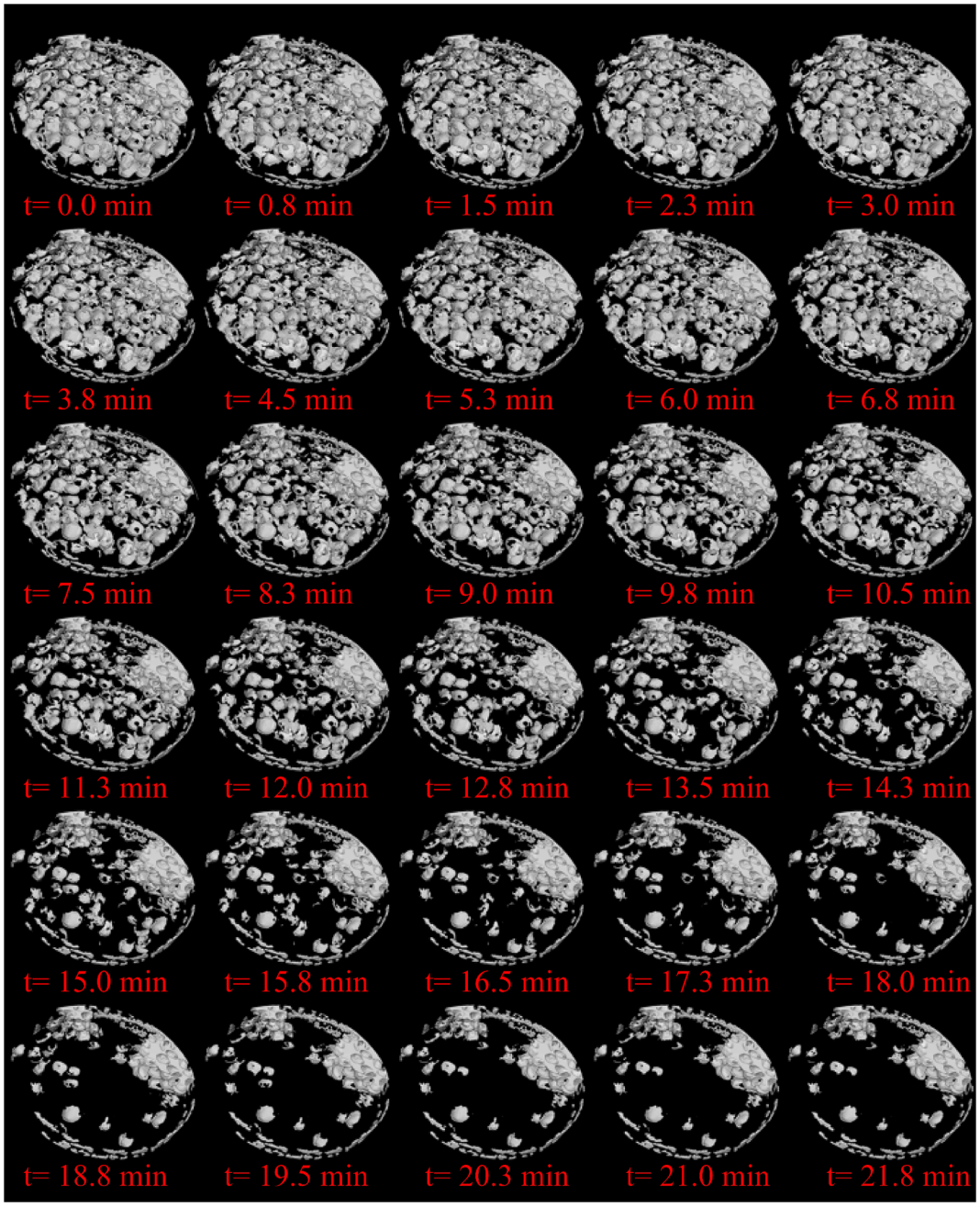

Fig. 3. Volume rendering images of hydrate during dissociation for a vertical section of the specimen for the depressurization experiment from beginning of the test to t = 22.5 min, time-lapse between images is 45 s.

Both gases form structure I clathrate hydrates with similar solubility and diffusivity properties [37,38]. Xenon hydrate has much lower equilibrium pressure compared to Methane hydrate. For example, the equilibrium pressure for Methane hydrate is 7.1 MPa at 10° C whereas it is 0.4 MPa for Xenon hydrate at the same temperature [28,39].

The chamber of the flow cell used in this study was machined using polyether ether ketone (PEEK) material, a strong material that has excellent x-ray attenuation. The cylindrical cell has a height of 70.2 mm and an inner diameter of 9.7 mm, and is capable of sustaining an internal pressure of 150 MPa (Fig. 1a). A cooling coil connected to a commercial cooling unit and is attached to the base plate of the cell. A circulated refrigerant gas is used to cool the cell, and a thermocouple

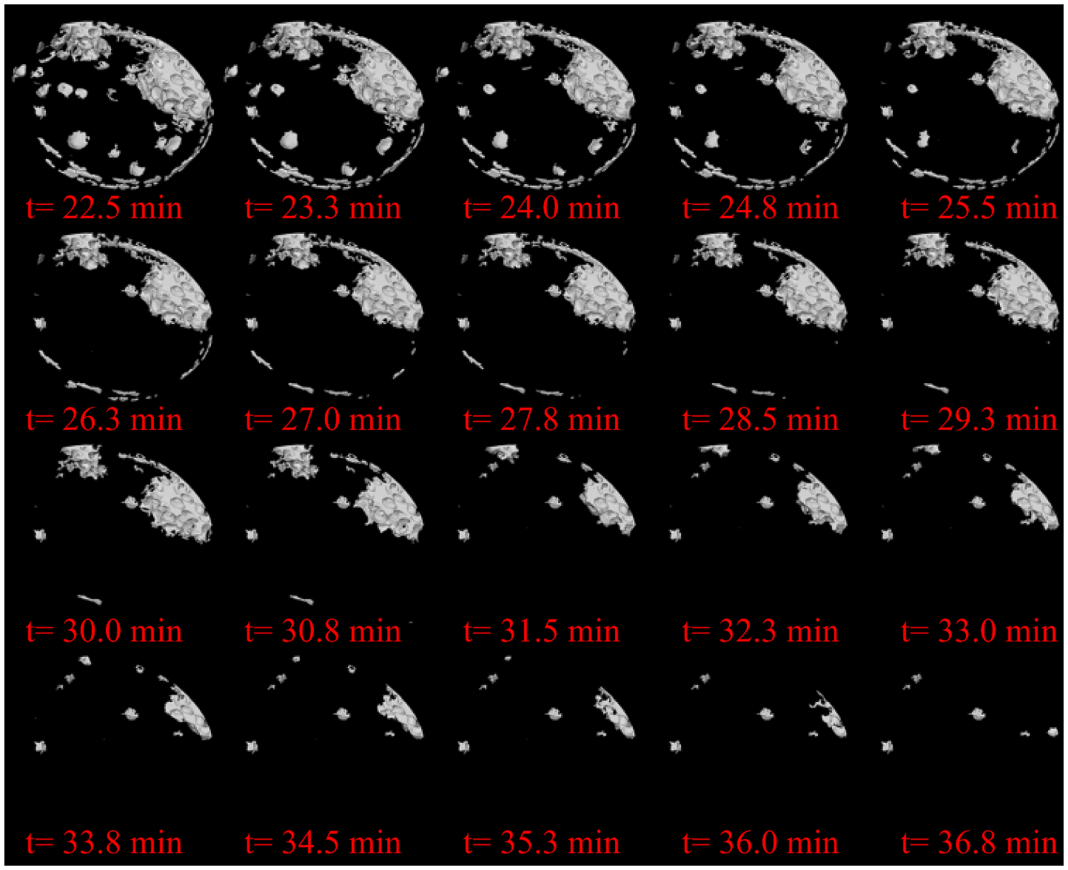

Fig. 4. Volume rendering images of hydrate during dissociation for a vertical section of the specimen for the depressurization experiment from t = 22.5 min to t = 37.5 min, time-lapse between images is 45 s.

housed in the top end plate is used to control the temperature inside the cell (Fig. 1a). An acrylic chamber and foam thermal insulation is used to isolate the cell and preserve the temperature within the cell (Fig. 1a). The bottom port is connected to a pressure regulator connected to Xenon gas source.

ASTM 20–30 Ottawa silica sand was used in this study. It has grain size between US sieve #20 (0.841 mm) and sieve #30 (0.595 mm), obtained from the US Silica Company. It has a specific gravity of solids of 2.65. The sand was partially saturated with a 4% by weight KI-brine solution (initial KI saturation = 52%) to enhance contrast in SMT images. Two steel meshes with 0.420 mm opening size were installed near the top and bottom ports to prevent sand migration. A plastic spacer and a stainless steel spring were placed on the top of the upper steel mesh to provide surcharge pressure at the top of the specimen. Xenon gas was then injected through the bottom port of the cell to displace water to reduce the initial degree of saturation.

3. 3D synchrotron micro-computed tomography (SMT)

X-ray computed tomography (CT) is a powerful non-destructive imaging technique in which the x-ray beam of a CT scanner impinges a rotating object and the collected attenuation data are used to reconstruct a 3D volume image of the object. 3D SMT is an enhancement to industrial CT with the utilization of a monochromatic x-ray beam, which eliminates beam-hardening artifacts and enables tuning photon energy [40–44]. In previous studies, both CT [45,46] and SMT [37,38,47] imaging were used to study gas hydrate dissociation and emergent phenomena in sandy sediments. However, the use of a monochromator in SMT greatly reduces the flux and increases data acquisition time, since it only transmits about 0.1% of the beam [48]. Alternatively, a grazing incidence mirror and an x-ray absorbing foil can be used instead of the monochromator to eliminate high and low energy x-ray photons. This improvement is known as pink beam synchrotron micro-computed tomography (PSMT), and can yield an x-ray flux three orders of magnitude higher than the monochromatic beam [48]. Therefore, the use of PSMT reduces data acquisition time

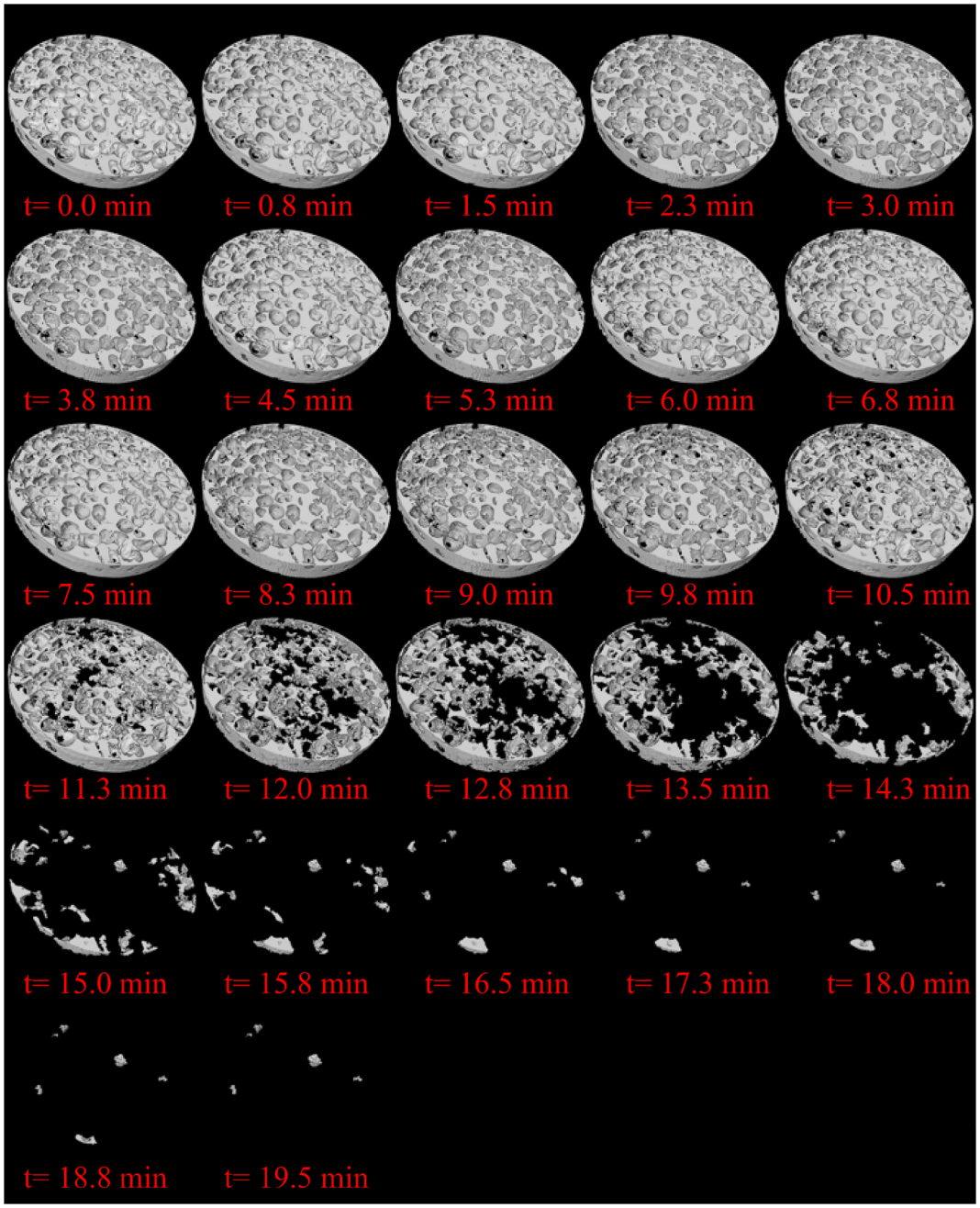

Fig. 5. Volume rendering images of hydrate during dissociation for a vertical section of the specimen for the thermal stimulation experiment from beginning of the test to t = 22.5 min, time-lapse between images is 45 s.

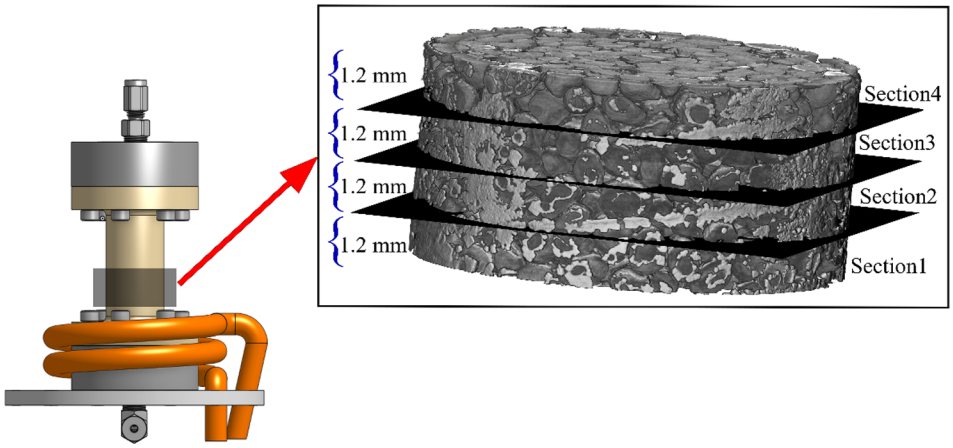

Fig. 6. Specimen scanned region and divided vertical sections (specimen inner diameter is 9.2 mm).

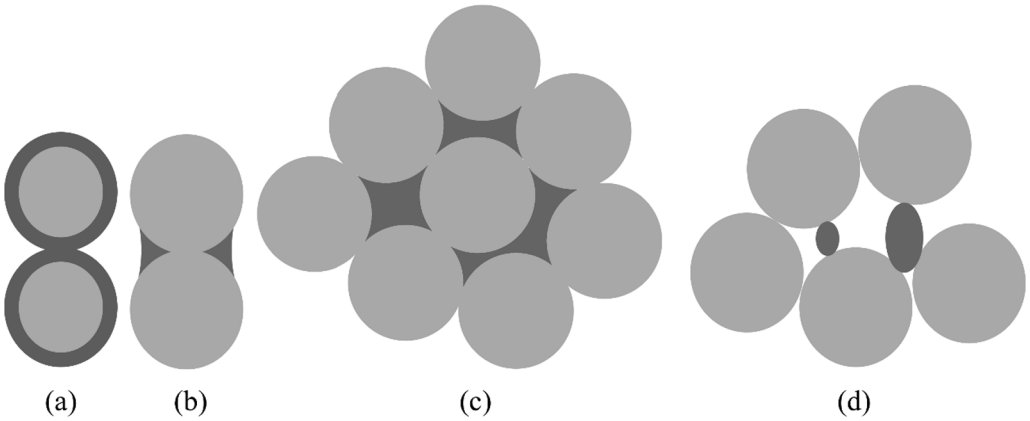

Fig. 7. Schematic of different hydrate pore habit: (a) surface coating; (b) cementing; (c) pore filling; and (d) load bearing.

significantly and makes an ideal option for in-situ monitoring of dynamic studies [49,50].

In this study, PSMT images were acquired at Beamline 13D of the Advanced Photon Source (APS), Argonne National Laboratory (ANL), IL, USA. The experimental setup in beamline 13D at APS is shown in Fig. 1b. Two dissociation experiments were performed in this study; one with hydrates dissociating by depressurization and one with hydrates dissociating by thermal stimulation. For the depressurization experiment, the cell was cooled to 10 ± 1° C temperature and Xenon gas was injected at an initial pressure of 1.9 MPa to initiate hydrate formation. After one hour of hydrate formation, hydrate dissociation was triggered through depressurization by closing the inlet valve from the gas source and releasing Xenon gas to the atmosphere. After all hydrates were dissociated, Xenon gas was injected again at an initial pressure of 1.9 MPa to form hydrates for the thermal stimulation experiment. After three hours of hydrate formation at a temperature of 14° C, the temperature was increased so the pressure–temperature conditions are below Xenon hydrate equilibrium conditions. Fig. 2a depicts hydrate phase boundary and experimental pressure–temperature measurments, while Fig. 2b depicts the change of temperature, pressure, and equilibrium pressure during hydrate dissociation for the thermal stimulation experiment. Xenon hydrate equilibrium conditions were interpolated from the results of Ewing and Ionescu [39] and Ohgaki et al. [51].

During dissociation, continuous full 3D PSMT images were acquired. Images were collected in pink beam mode with 1 mm Aluminum absorber and 1.5 milli-radian mirror angle and an exposure time of 8 ms. Each scan took approximately 45 s to complete (12 s collection time and the remaining time is for saving raw data to a file server), and a total of 60 scans were acquired. Each raw image had a size of 1920 pixel × 1920 pixel × 880 pixel, with a resolution of approximately 5.4 μm/voxel. All scans were acquired near the bottom third of the specimen and did not cover the full height.

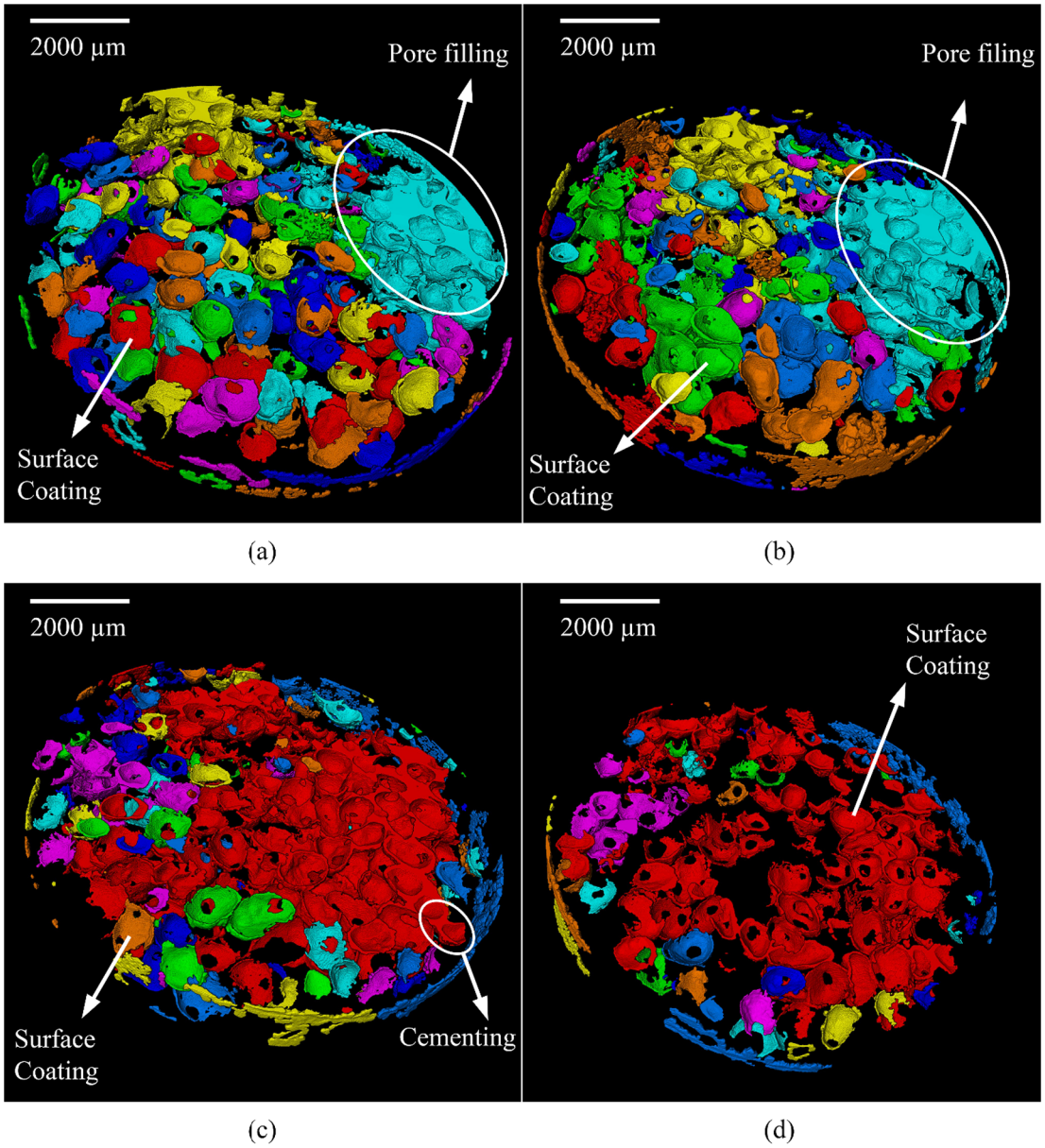

Fig. 8. Initial hydrate pore habit distribution highlighted in volume rendering images for the depressurization experiment for: (a) Section 1; (b) Section 2; (c) Section 3; and (d) Section 4 of the specimen.

4. Results

4.1. Image analysis

Raw images were pre-processed and reconstructed to 3D 16-bit integer volumes using the multi-threading software package "tomoRecon" [52]. Reconstructed 3D volumes were processed and segmented using Avizo 9.7 software [53]. Median filter was used to reduce the contrast and soften the edges of the grayscale images by setting the pixel value to the median of the neighboring pixels [53]. Interactive thresholding module was used to segment the images by selecting values of image intensity ranges for each phase [53]. Figs. 3 and 4 display volume rendering images of the hydrate phase during dissociation for a vertical cross-section of the specimen for the depressurization experiment with a time-lapse of 45 s, while Fig. 5 presents the volume rendering images during hydrate dissociation for the thermal stimulation experiment.

4.2. Initial hydrate distribution and pore habit

The specimen was divided into four equal vertical sections (Fig. 6), with initial porosity of the host sediments ranging from 0.410 (Section

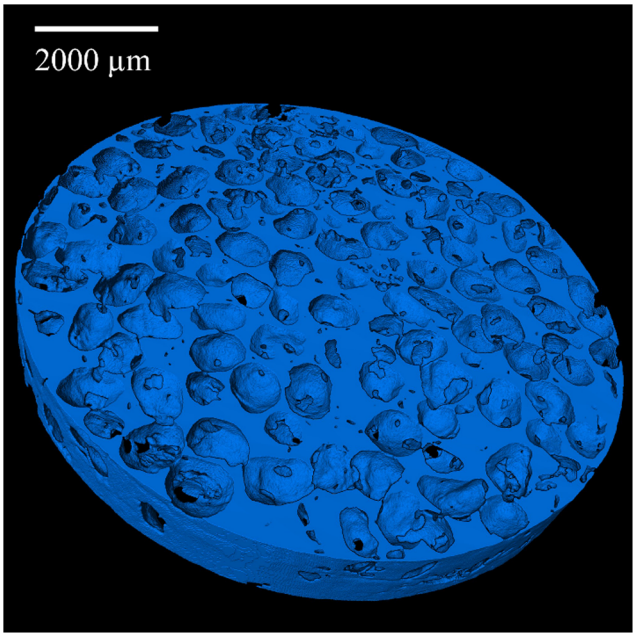

Fig. 9. Volume rendering image for section 1of the thermal stimulation experiment showing the pore-filling pore habit.

Table 1
Porosity and initial hydrate saturation values for the four sections of the depressurization and thermal stimulation experiments.

Section	Porosity	Initial hydrate degree of saturation, S (%)	
		Depressurization	Thermal stimulation
1	0.418	26.6	87.1
2	0.424	28.3	85.3
3	0.411	23.9	79.9
4	0.428	9.9	73.2

3) to 0.428 (Section 4). Hydrate pore habit refers to where hydrates are distributed within the pores of the host sediments, which can cause fundamental changes to the physical properties of hydrate-bearing sediments such as permeability, shear strength, and stiffness [54,55]. There are mainly four common hydrate pore habits that are discussed in the literature: surface coating, cementing, pore filling, and load bearing. Surface coating hydrates form as films on the surface of host sediment particles and are usually associated with excess gas condition. Cementing hydrates form at contacts between host sediment particles while pore filling hydrates form at the surface of host sediment particles and grow outward filling the pore space. Finally, load bearing refers to hydrates at high hydrate saturation where they can carry some of the load applied to the host sediments. A schematic of the different hydrate pore habit is depicted in Fig. 7. Initial hydrate saturation for the depressurization experiment ranged from 9.9% (Section 4) to 28.3% (Section 2). Hydrates were distributed heterogeneously with multiple pore habits, which is in agreement with observations from natural hydrate [56,57] and laboratory studies [58,59]. A combination of cementing, pore-filling, and surface coating pore habits were observed in Sections 1 and 2 (Fig. 8a and b), while the pore habit in Sections 3 and 4 were predominantly surface coating (Fig. 8 c and d). For the thermal stimulation experiment, the initial hydrate saturation was significantly higher than the depressurization experiment ranging from 73.2% for Section 4 and 87.1% for Section 1. The predominant pore habit for all four sections was pore filling (Fig. 9). Table 1 lists porosity and initial hydrate saturation values for the four sections of the depressurization and thermal stimulation experiments.

4.3. Hydrate volume and surface area

According to hydrate sphericity assumptions proposed by Kim et al. [28], the change of hydrate surface area with (hydrate volume)$^{2/3}$ should be linear during dissociation. Fig. 10 shows scatter plots of total hydrate interfacial area (total surface area), hydrate-sand interfacial area, and hydrate-gas interfacial area with (hydrate volume)$^{2/3}$ measured from the 3D PSMT images of the depressurization experiment. Hydrate-gas interfacial area represents the total surface area of the hydrate phase in contact with the gas phase. Similarly, hydrate-sand interfacial area represents the total surface area of the hydrate phase in contact with the sand phase, while the total interfacial area is the sum of hydrate-gas interfacial area and hydrate-sand interfacial area and is a measure of the total surface area of the hydrate phase. The reported interfacial area measurements do not account for the micro-pores within hydrate structures which cannot be detected at the resolution of this study. These micro-pores have been observed by 3D SMT imaging [60] and field-emission scanning electron microscopy [61] with sizes ranging from sub-micron to few microns. That said, the reported interfacial areas can be overestimates of the actual areas. Referring to Fig. 10, good linear fits can be observed for low hydrate volumes up to a certain threshold, after which, interfacial area deviate from linearity. This threshold corresponds to 7%, 6%, and 8% hydrate saturation for total interfacial area (Fig. 10b), hydrate-gas interfacial area (Fig. 10c), and hydrate-sand interfacial area (Fig. 10d), respectively. Coefficients of determination (R^2) and root mean square errors (RMSE) values for the three models are also presented in Fig. 10. R^2 values ranged from 0.16 (hydrate-sand interfacial area) to 0.35 (hydrate-gas interfacial area), while RMSE values ranged from 2.23 (hydrate-gas interfacial area) to 6.28 (total interfacial area). Therefore, hydrate surface area can be estimated to be linear with (hydrate volume)$^{2/3}$ during hydrate dissociation in porous media for hydrate saturation less than a certain threshold (8% in this study), based on direct observations and measurements from 3D PSMT images.

Additionally, best fit polynomials between hydrate volume and interfacial areas were investigated. Fig. 11 presents scatter plots of total hydrate interfacial area, hydrate-sand interfacial area, and hydrate-gas interfacial area with hydrate volume, along with the best quadratic fit models for the depressurization experiment. As shown in Fig. 11, quadratic fit models provide excellent prediction of interfacial area with R^2 values higher than 0.98. Therefore, it is suggested that (hydrate volume)^2 can give better estimation of hydrate surface area than (hydrate volume)$^{2/3}$ based on results obtained from this study. Fig. 12 compares hydrate dissociation rates measured experimentally from PSMT images with predicted dissociation rates calculated from Eq. (1) with time for the depressurization experiment. Hydrate surface area are estimated once to be linear with $v^{2/3}$ (circles in Fig. 12) and once according to the polynomial fits provided in Fig. 11 (squares in Fig. 12). Estimating hydrate surface area according to the polynomials reported in this study improved the prediction of hydrate dissociation rates (RMSE = 0.44) compared to estimating hydrate surface area to be

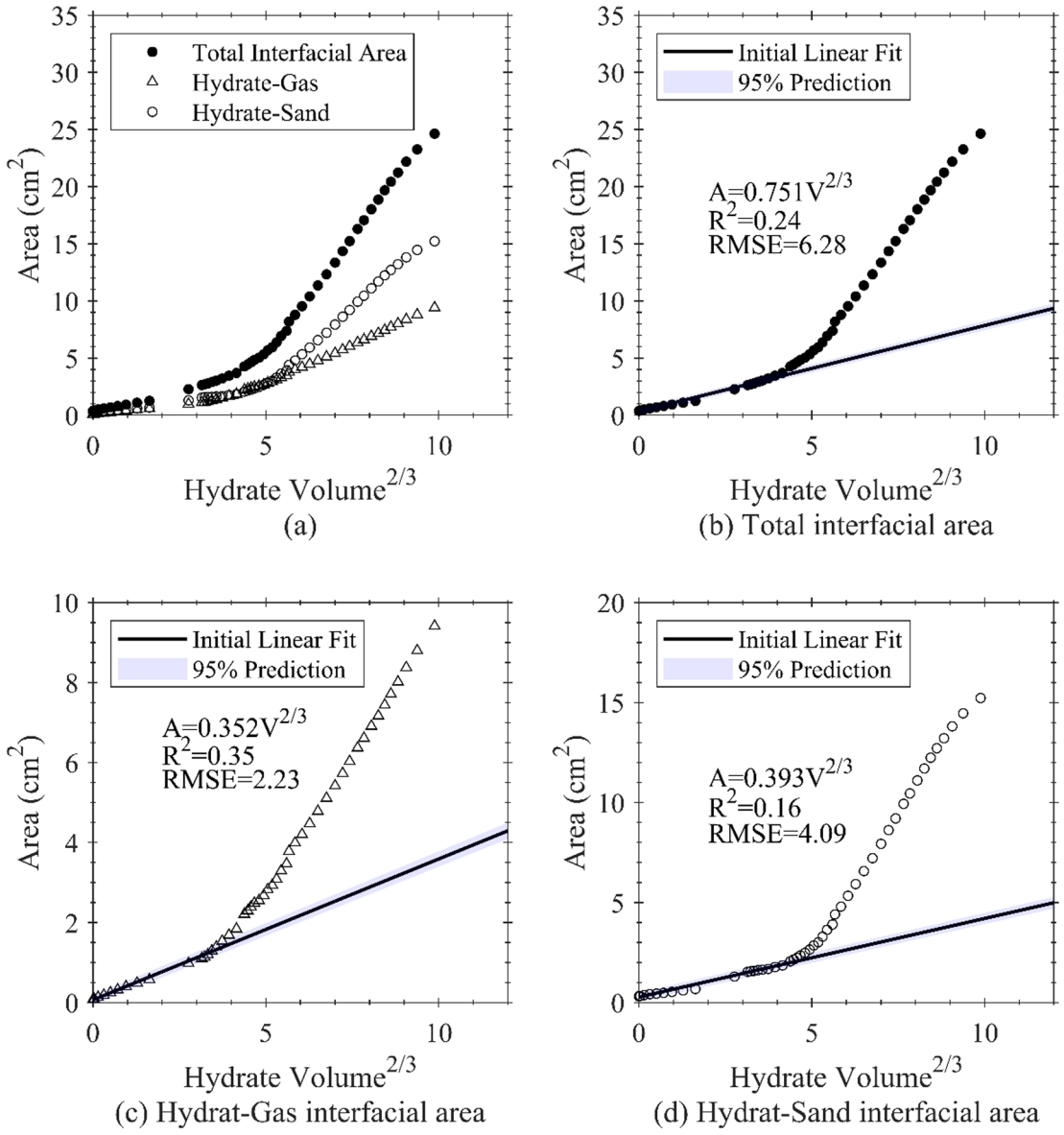

Fig. 10. Variation of (hydrate volume)$^{2/3}$ versus: (a) combined interfacial area measurements; (b) total hydrate interfacial area; (c) hydrate-gas interfacial area; and (d) hydrate-sand interfacial area along with initial best fit lines and 95% prediction bands for the depressurization experiment.

linear with $v^{2/3}$ (RMSE = 0.79).

Fig. 13 shows scatter plots of total hydrate interfacial area, hydrate-sand interfacial area, and hydrate-gas interfacial area with (hydrate volume)$^{2/3}$ measured from the 3D PSMT images for the thermal stimulation experiment. Fig. 13 also presents R^2 and RMSE values for the three linear models. Similar to the depressurization experiment, good linear fits can be observed for hydrate volumes smaller than a certain threshold, after which, interfacial area begins to deviate from linearity. This threshold corresponds to 28% hydrate saturation for total interfacial area (Fig. 13b) and hydrate gas interfacial area (Fig. 13c), and 12% hydrate saturation for hydrate-sand interfacial area (Fig. 13d). Total interfacial area and hydrate-gas interfacial area showed better overall linearity with (hydrate volume)$^{2/3}$ in the thermal stimulation experiment compared to the depressurization experiment with significantly higher R^2 values. Additionally, best fit polynomials between hydrate volume and interfacial areas were investigated. Fig. 14 presents scatter plots of total hydrate interfacial area, hydrate-sand interfacial area, and hydrate-gas interfacial area with hydrate volume, along with the best cubic fit models, which were found to best estimate interfacial area with hydrate volume. These cubic fit models provide excellent prediction of interfacial area with R^2 values higher than 0.98.

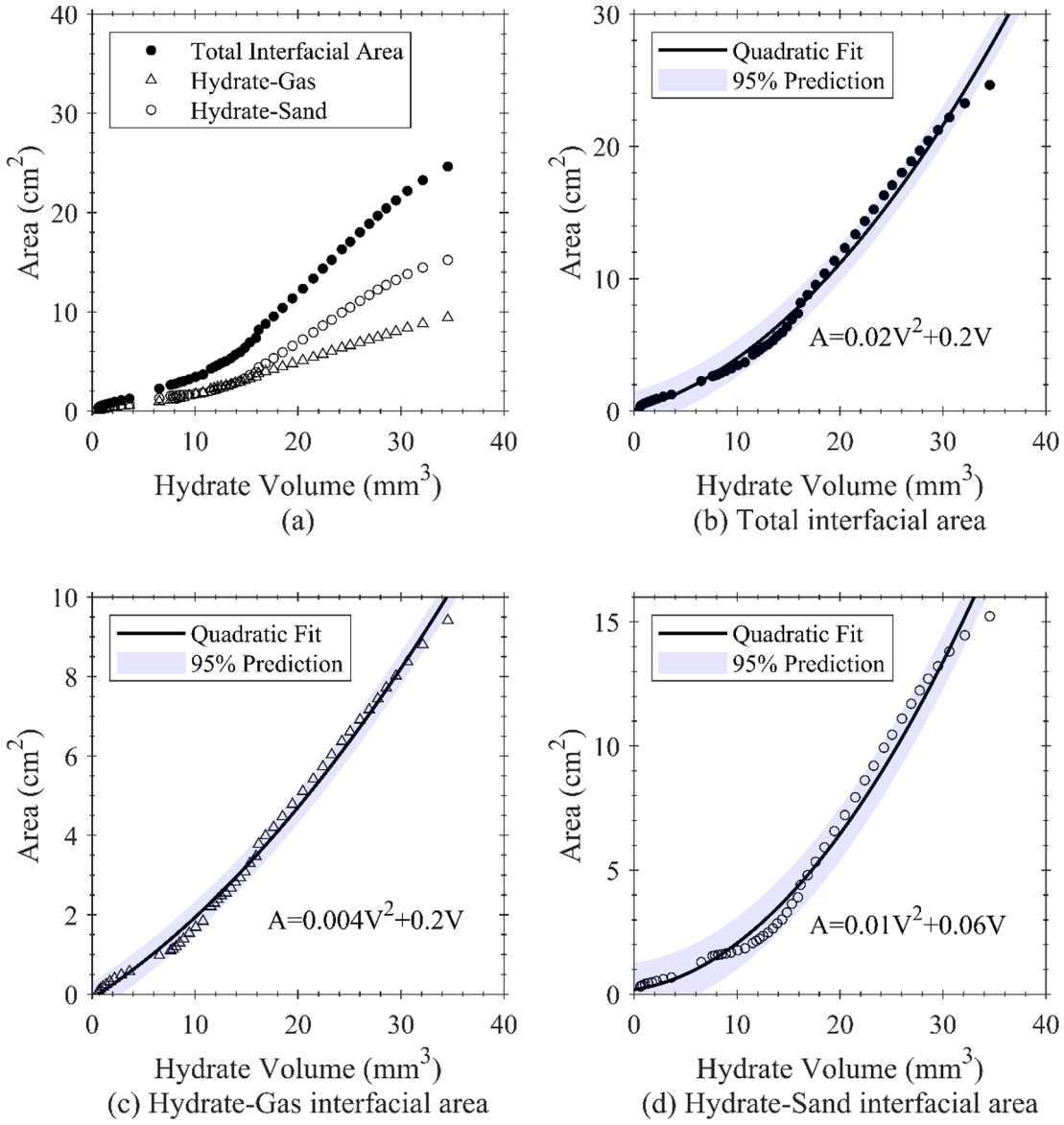

Fig. 11. Variation of (a) combined interfacial area measurements; (b) total hydrate interfacial area; (c) hydrate-gas interfacial area; and (d) hydrate-sand interfacial area with hydrate volume along with best quadratic fit and 95% prediction bands for the depressurization experiment.

4.4. Hydrate specific area and dissociation rate

Fig. 15a displays the change in hydrate specific area with time during dissociation for Sections 1 through 4. For Sections 1 and 2, hydrate specific area decreased with time, which indicates that hydrates with higher specific area dissociate first resulting in a reduction of the total specific area of that section (Fig. 15a). Therefore, hydrates with surface coating pore habit are expected to dissociate faster than hydrates with pore-filling pore habits. This also can be observed in the volume rendering images depicted in Fig. 16a-e that shows surface coating hydrates dissociated before pore filling hydrates. For Sections 3 and 4, hydrates are predominantly surface coating (Fig. 8c and e) and therefore have higher specific area compared to Sections 1 and 2 (Fig. 15a). During dissociation, specific area of Sections 3 and 4 fluctuated around a constant value with no obvious trend (Fig. 15a) since most hydrates in these sections have the same pore habit (surface coating). Fig. 15b depicts the change in hydrate dissociation rate with time during hydrate dissociation for Sections 1 and 2, and Sections 3 and 4. Hydrate dissociation rates were measured experimentally by dividing the change in the measured hydrate volume by the scan time (45 s) between consecutive 3D PSMT images. Higher dissociation rates are observed for Sections 3 and 4 in comparison with Sections 1 and 2,

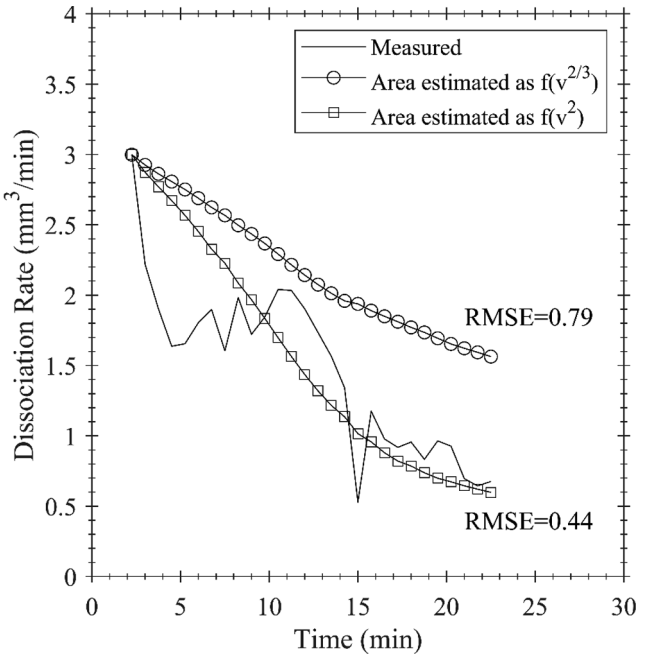

Fig. 12. Change of measured dissociation rate with predicted dissociation rate according to Eq. (1) with time for the depressurization experiment.

which is attributed to the higher specific area in Sections 3 and 4 which means they have more surface to dissociate at (Fig. 15a).

During the depressurization experiment, the temperature and pressure were kept constant, and therefore, hydrate equilibrium pressure also remained constant throughout the test. However, during hydrate dissociation by thermal stimulation, pressure, temperature, and therefore, hydrate equilibrium pressure were changing during the test (see Fig. 2). In this study, multiple linear regression analysis was conducted to propose a simple model that relates hydrate dissociation rate with hydrate saturation (S), absolute temperature (T), pressure (P), and the hydrate equilibrium pressure (P_e). The least-square method was used to estimate regression coefficients that minimize the vertical deviation from each data point to the regression line. The p-value is used to assess the significance of each regression coefficient. A low p-value means that the null hypothesis that the coefficient is equal to zero can be rejected. In other words, a predictor with a low p-value is considered significant to the model, because changing the value of its coefficient changes the response of the model. The estimated regression coefficients for each predictor in the model, along with their corresponding p-value are listed in Table 2. The prediction model had an R^2 value of 0.94 and an RMSE value of 0.88. The change of measured and predicted hydrate dissociation rate with hydrate saturation along with the linear regression model for the thermal stimulation experiment are depicted in Fig. 17. It can be observed from Fig. 17 that the hydrate dissociation rate remains almost constant at the start of the dissociation process. This constant dissociation rate can be attributed to the exposure of the micro-pores within hydrates, which compensates for the loss in hydrate surface area during dissociation.

5. Conclusions

This paper employed dynamic 3D PSMT imaging in studying hydrate surface area evolution during Xenon hydrate dissociation. Hydrates were formed inside a high-pressure low-temperature flow cell filled with partially saturated ASTM 20–30 Ottawa silica sand and two hydrate dissociation experiments were conducted. The cell was cooled to 10° C temperature in the first experiment and to 14° C in the second experiment. Xenon gas was injected at an initial pressure of 1.9 MPa for both experiments. Hydrate dissociation was triggered through depressurization in the first experiment by closing the inlet valve from the gas source and releasing Xenon gas to the atmosphere and by thermal stimulation in the second experiment. During dissociation, continuous full 3D tomography images were acquired where each scan took 45 s to complete. A combination of cementing, pore-filling, and surface coating initial pore habits were observed for the depressurization experiment, while pore-filling pore habit was predominant in the thermal stimulation experiment. Surface coating hydrates dissociate faster than hydrates with pore-filling pore habit. This is explained by the higher specific area in the surface coating hydrates, which allows for more surface for hydrates to dissociate it. Results suggest that with a combination of hydrate pore habit formed within the 3D porous media, estimation of hydrate surface area as a linear relationship with (hydrate volume)$^{2/3}$ is best for hydrate saturation less than a specific threshold value. The value of this threshold varies depending on the dissociation method and the driving dissociation force and was found to be 7% for the depressurization experiment and 28% for the thermal stimulation experiment. (hydrate volume)^2 was found to better estimate hydrate interfacial area compared to (hydrate volume)$^{2/3}$ in the depressurization experiment, while (hydrate volume)^3 provided better estimates of the interfacial area for the thermal stimulation experiment. Findings of this study along with dynamic SMT imaging technique can be used to improve hydrate dissociation models and predictability of gas production from natural hydrate reservoirs. Finally, multiple linear regression analysis was conducted to predict hydrate dissociation rate variation using hydrate saturation, temperature pressure, and hydrate equilibrium pressure as predictors. The model provided good estimates of dissociation rate with an R^2 value of 0.94 and an RMSE value of 0.88.

CRediT authorship contribution statement

Zaher A. Jarrar: Conceptualization, Methodology, Investigation, Software, Formal analysis, Writing - original draft. **Khalid A. Alshibli:** Funding acquisition, Data curation, Conceptualization, Methodology, Investigation, Writing - review & editing, Supervision. **Riyadh I. Al-Raoush:** Funding acquisition, Project administration, Conceptualization, Methodology, Investigation, Supervision, Resources, Writing - review & editing. **Jongwon Jung:** Funding acquisition, Conceptualization, Methodology, Investigation, Writing - review & editing.

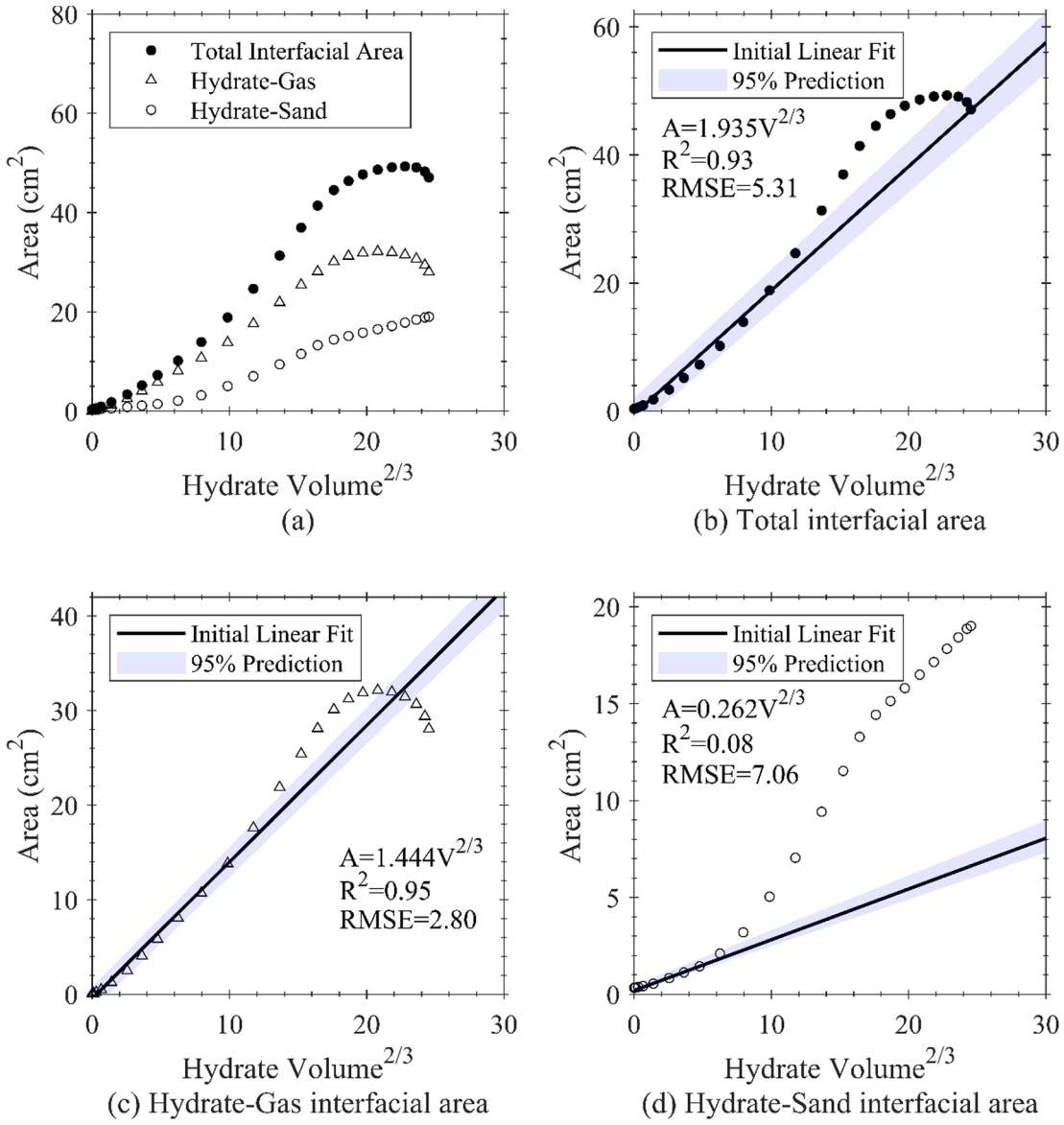

Fig. 13. Variation of (hydrate volume)$^{2/3}$ versus: (a) combined interfacial area measurements; (b) total hydrate interfacial area; (c) hydrate-gas interfacial area; and (d) hydrate-sand interfacial area along with initial best fit lines and 95% prediction bands for the thermal stimulation experiment.

Declaration of Competing Interest

The authors declare that they have no known competing financial interests or personal relationships that could have appeared to influence the work reported in this paper.

Acknowledgments

This publication was made possible by partial funding from NPRP grant # NPRP8-594-2-244 from the Qatar national research fund (a member of Qatar Foundation) and the Institute for a Secure and Sustainable Environment (ISSE), University of Tennessee-Knoxville, USA. Any opinions, findings, and conclusions or recommendations expressed in this material are those of the authors and do not necessarily

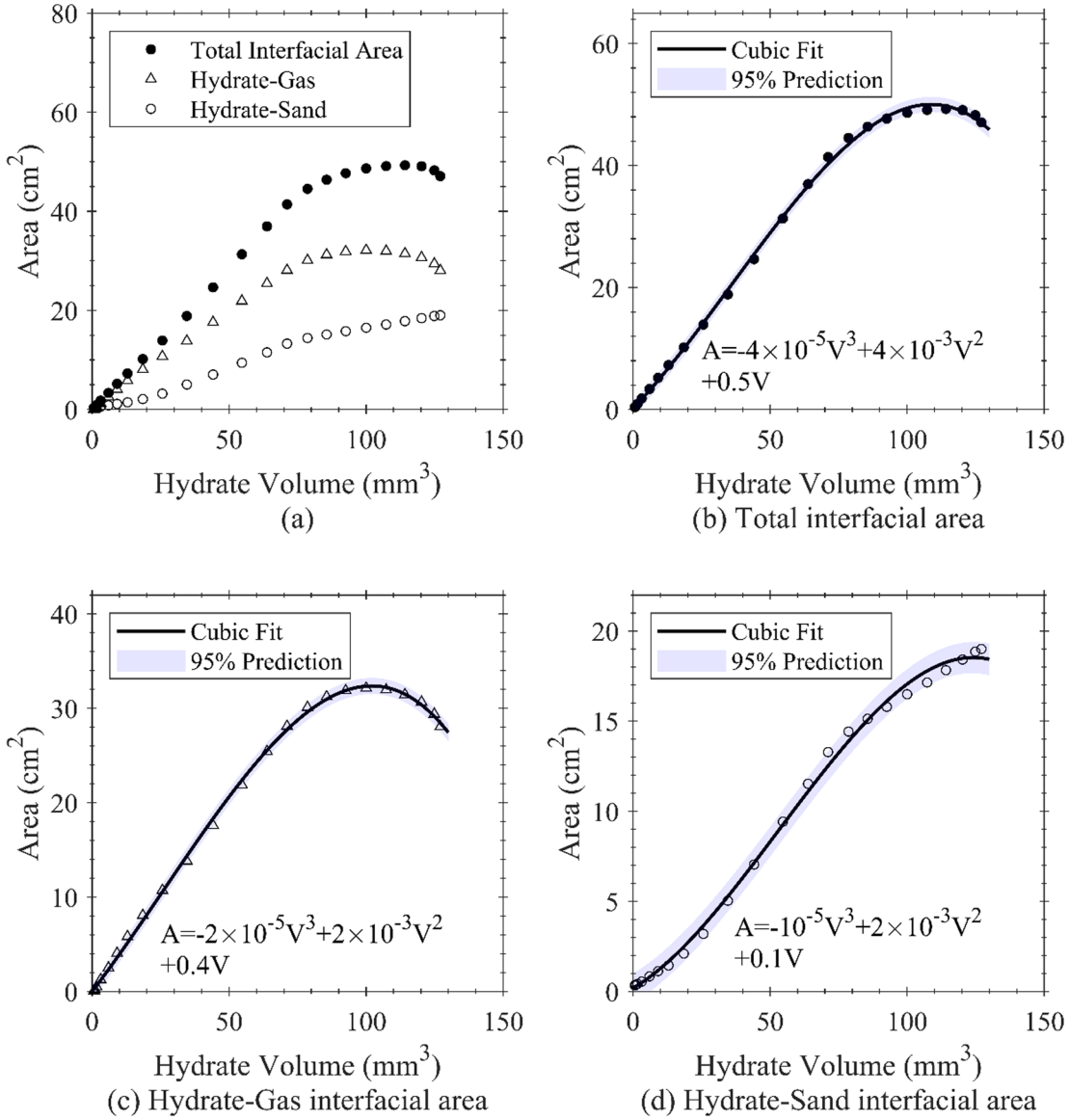

Fig. 14. Variation of (a) combined interfacial area measurements; (b) total hydrate interfacial area; (c) hydrate-gas interfacial area; and (d) hydrate-sand interfacial area with hydrate volume along with best cubic fit and 95% prediction bands for the thermal stimulation experiment.

reflect the views of funding agencies. The authors would like to thank Mr. Wadi Imseeh for his help during scanning and Mr. Jamal Hannun for his help in interfacial area analysis. This paper used resources of the Advanced Photon Source (APS), a U.S. Department of Energy (DOE) Office of Science User Facility operated for the DOE Office of Science by Argonne National Laboratory (ANL) under Contract No. DE-AC02-06CH11357. The PSMT images presented in this paper were collected using the x-ray Operations and Research Beamline Station 13-BMD at Argonne Photon Source (APS), ANL. We thank Dr. Mark Rivers of APS for help in performing the PSMT scans. We also acknowledge the support of GeoSoilEnviroCARS (Sector 13), which is supported by the National Science Foundation, Earth Sciences (EAR-1128799), and the DOE, Geosciences (DE-FG02-94ER14466). The authors would also like to thank the anonymous reviewers who contributed with comments and suggestions to improve this paper.

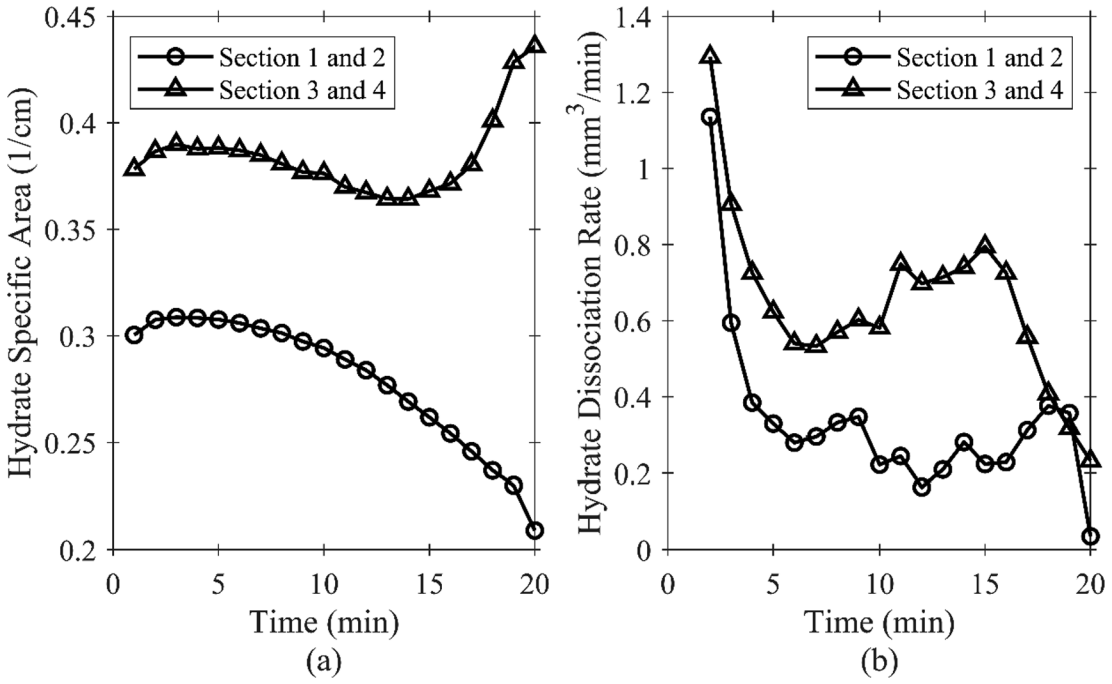

Fig. 15. Change of (a) hydrate specific area; and (b) hydrate dissociation rate with time during dissociation for the depressurization experiment.

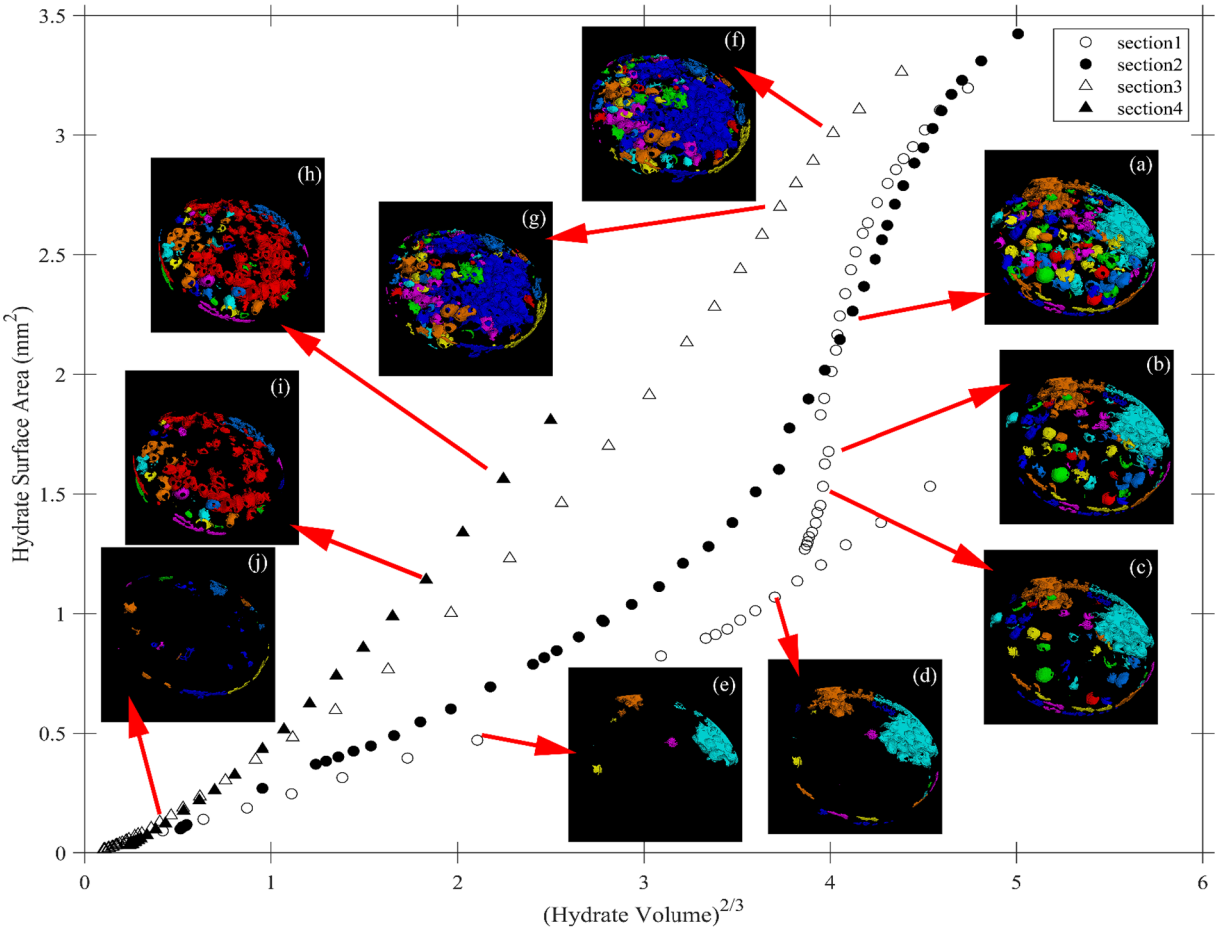

Fig. 16. Change of hydrate surface area with (hydrate volume)$^{2/3}$ during hydrate dissociation for the four vertical sections of the specimen for the depressurization experiment along with volume rendering images at selected points.

Table 2
Results of multivariable linear regression of dissociation rate for the thermal stimulation experiment.

Parameter	Coefficient Estimate	p-value
T	−457.4	0.05
P	5520.2	< 0.01
P_e-P	5007.8	< 0.01
S^3	-9.5×10^{-5}	< 0.01
Statistical Constant	127803.2	N/A

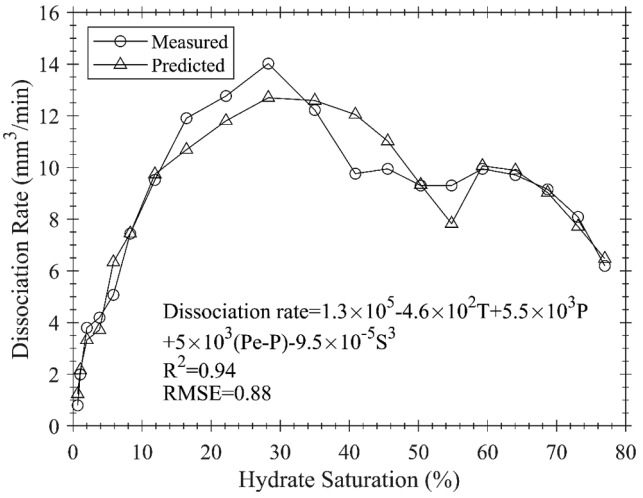

Fig. 17. Change of measured and predicted hydrate dissociation rate with hydrate saturation along with the linear regression model for the thermal stimulation experiment.

References

[1] Bonnefoy O, Gruy F, Herri JM. Van der Waals interactions in systems involving gas hydrates. Fluid Phase Equilib 2005;231(2):176–87.
[2] Sloan EDJ. Fundamental principles and application of natural gas hydrates. Nature 2003;426:353–63.
[3] Ye Y, Liu C. Natural gas hydrates: experimental techniques and their applications. Springer Science & Business Media; 2012.
[4] Max MD, Johnson AH, Dillon WP. Natural gas hydrate-arctic ocean deepwater resource potential. Springer; 2013.
[5] Sloan Jr ED, Koh CA. Clathrate hydrates of natural gases. CRC Press; 2007.
[6] Kvenvolden KA. A review of the geochemistry of methane in natural gas hydrate. Org Geochem 1995;23(11):997–1008.
[7] Merey S, Al-Raoush RI, Jung J, Alshibli KA. Comprehensive literature review on CH4-CO2 replacement in microscale porous media. J Petrol Sci Eng 2018;171:48–62.
[8] Chong ZR, Yang SHB, Babu P, Linga P, Li X-S. Review of natural gas hydrates as an energy resource: prospects and challenges. Appl Energy 2016;162:1633–52.
[9] Xu C-G, Li X-S. Research progress on methane production from natural gas hydrates. RSC Adv 2015;5(67):54672–99.
[10] Chen L, Feng Y, Kogawa T, Okajima J, Komiya A, Maruyama S. Construction and simulation of reservoir scale layered model for production and utilization of methane hydrate: the case of Nankai Trough Japan. Energy 2018;143:128–40.
[11] Konno Y, Masuda Y, Hariguchi Y, Kurihara M, Ouchi H. Key Factors for depressurization-induced gas production from oceanic methane hydrates. Energy Fuels 2010;24(3):1736–44.
[12] Konno Y, Fujii T, Sato A, Akamine K, Naiki M, Masuda Y, et al. Key findings of the world's first offshore methane hydrate production test off the coast of Japan: toward future commercial production. Energy Fuels 2017;31(3):2607–16.
[13] Minagawa H, Ito T, Kimura S, Kaneko H, Noda S, Narita H. Depressurization and electrical heating of hydrate sediment for gas production. Proceedings of the International Offshore and Polar Engineering Conference. 2015. p. 82–8.
[14] Moridis GJ, Collett TS, Boswell R, Hancock S, Rutqvist J, Santamarina C, et al. Gas hydrates as a potential energy source: state of knowledge and challenges. In: Lee JW, editor. Advanced Biofuels and Bioproducts. New York, NY: Springer New York; 2013. p. 977–1033.
[15] Daraboina N, Malmos C, von Solms N. Synergistic kinetic inhibition of natural gas hydrate formation. Fuel 2013;108:749–57.
[16] Hyodo M, Li Y, Yoneda J, Nakata Y, Yoshimoto N, Kajiyama S, et al. A comparative analysis of the mechanical behavior of carbon dioxide and methane hydrate-bearing sediments. Am Mineral 2014;99(1):178–83.
[17] Liu W, Luo T, Li Y, Song Y, Zhu Y, Liu Y, et al. Experimental study on the mechanical properties of sediments containing CH4 and CO2 hydrate mixtures. J Nat Gas Sci Eng 2016;32:20–7.
[18] Jung JW, Santamarina JC. CH4-CO2 replacement in hydrate-bearing sediments: A pore-scale study. Geochem Geophys Geosyst 2010;11(12).
[19] Jung JW, Espinoza DN, Santamarina JC. Properties and phenomena relevant to CH4-CO2 replacement in hydrate-bearing sediments. J Geophys Res: Solid Earth 2010;115(B10).
[20] Huang Y-J, Wu C-Y, Hsieh B-Z. Effect of fluid saturation on gas recovery from class-3 hydrate accumulations using depressurization: a case study of the yuan-an ridge site in southwestern offshore Taiwan. Energy Proc 2016;97:310–7.
[21] Collett T, Bahk J-J, Baker R, Boswell R, Divins D, Frye M, et al. Methane hydrates in nature—Current knowledge and challenges. J Chem Eng Data 2015;60(2):319–29.
[22] Windmeier C, Oellrich LR. Theoretical study of gas hydrate decomposition kinetics—Model development. J Phys Chem A 2013;117(40):10151–61.
[23] Oyama H, Konno Y, Masuda Y, Narita H. Dependence of depressurization-induced dissociation of methane hydrate bearing laboratory cores on heat transfer. Energy Fuels 2009;23(10):4995–5002.
[24] Selim MS, Sloan ED. Heat and mass transfer during the dissociation of hydrates in porous media. AIChE J 1989;35(6):1049–52.
[25] Hong H, Pooladi-Darvish M, Bishnoi PR. Analytical Modelling of Gas Production From Hydrates in Porous Media. PETSOC-03-11-05 2003;42(11):45–56.
[26] Gamwo IK, Liu Y. Mathematical modeling and numerical simulation of methane production in a hydrate reservoir. Ind Eng Chem Res 2010;49(11):5231–45.
[27] Jamaluddin AKM, Kalogerakis N, Bishnoi PR. Modelling of decomposition of a synthetic core of methane gas hydrate by coupling intrinsic kinetics with heat transfer rates. Can J Chem Eng 1989;67(6):948–54.
[28] Kim HC, Bishnoi PR, Heidemann RA, Rizvi SSH. Kinetics of methane hydrate decomposition. Chem Eng Sci 1987;42(7):1645–53.
[29] Yin Z, Chong ZR, Tan HK, Linga P. Review of gas hydrate dissociation kinetic models for energy recovery. J Nat Gas Sci Eng 2016;35:1362–87.
[30] Clarke M, Bishnoi PR. Determination of the activation energy and intrinsic rate constant of methane gas hydrate decomposition. Can J Chem Eng 2001;79(1):143–7.
[31] Moridis GJ, Seol Y, Kneafsey TJ. Studies of reaction kinetics of methane hydrate dissocation in porous media. 2005.
[32] Kneafsey TJ, Tomutsa L, Moridis GJ, Seol Y, Freifeld BM, Taylor CE, et al. Methane hydrate formation and dissociation in a partially saturated core-scale sand sample. J Petrol Sci Eng 2007;56(1):108–26.
[33] Chen X, Espinoza DN. Surface area controls gas hydrate dissociation kinetics in porous media. Fuel 2018;234:358–63.
[34] Chen X, Espinoza DN. Ostwald ripening changes the pore habit and spatial variability of clathrate hydrate. Fuel 2018;214:614–22.
[35] Jin Y, Nagao J, Hayashi J, Shimada W, Ebinuma T, Narita H. Observation of Xe hydrate growth at gas – ice interface by microfocus X-ray computed tomography. J Phys Chem C 2008;112(44):17253–6.
[36] Sell K, Saenger EH, Falenty A, Chaouachi M, Haberthür D, Enzmann F, et al. On the path to the digital rock physics of gas hydrate-bearing sediments–processing of in situ synchrotron-tomography data. Solid Earth 2016;7(4):1243–58.
[37] Yang L, Falenty A, Chaouachi M, Haberthür D, Kuhs WF. Synchrotron X-ray computed microtomography study on gas hydrate decomposition in a sedimentary matrix. Geochem Geophys Geosyst 2016;17(9):3717–32.
[38] Chaouachi M, Falenty A, Sell K, Enzmann F, Kersten M, Haberthür D, et al. Microstructural evolution of gas hydrates in sedimentary matrices observed with synchrotron X-ray computed tomographic microscopy. Geochem Geophys Geosyst 2015;16(6):1711–22.
[39] Ewing GJ, Ionescu LG. Dissociation pressure and other thermodynamic properties of xenon-water clathrate. J Chem Eng Data 1974;19(4):367–9.
[40] Kinney JH, Nichols MC. X-ray tomographic microscopy (XTM) using synchrotron radiation. Annu Rev Mater Sci 1992;22(1):121–52.
[41] Al-Raoush R. Change in microstructure parameters of porous media over representative elementary volume for porosity. Part Sci Technol 2012;30(1):1–16.
[42] Wildenschild D, Rivers ML, Porter ML, Iltis GC, Armstrong RT, Davit Y. Using synchrotron-based X-ray microtomography and functional contrast agents in environmental applications. In: Anderson SH, Hopmans JW, editors. Soil–water–root processes: advances in tomography and imaging. Madison, WI: The Soil Science Society of America, Inc.; 2013. p. 1–22.
[43] Al-Raoush RI. Experimental investigation of the influence of grain geometry on residual NAPL using synchrotron microtomography. J Contam Hydrol 2014;159:1–10.
[44] Alshibli KA, Reed AH. Advances in computed tomography for geomaterials: GeoX 2010. John Wiley & Sons; 2012.
[45] Lei L, Seol Y, Choi J-H, Kneafsey TJ. Pore habit of methane hydrate and its evolution in sediment matrix – Laboratory visualization with phase-contrast micro-CT. Mar Pet Geol 2019;104:451–67.
[46] Kneafsey TJ, Moridis GJ. X-Ray computed tomography examination and comparison of gas hydrate dissociation in NGHP-01 expedition (India) and Mount Elbert (Alaska) sediment cores: Experimental observations and numerical modeling. Mar Pet Geol 2014;58:526–39.
[47] Jarrar ZA, Al-Raoush RI, Hannun JA, Alshibli KA, Jung J. 3D synchrotron computed tomography study on the influence of fines on gas driven fractures in Sandy Sediments. Geomech Energy Environ 2018::100105.
[48] Rivers ML. High-speed tomography using pink beam at GeoSoilEnviroCARS. SPIE; 2016.
[49] Godinho JRA, Gerke KM, Stack AG, Lee PD. The dynamic nature of crystal growth in pores. Sci Rep 2016;6:33086.

[50] Andrew M, Menke H, Blunt MJ, Bijeljic B. The imaging of dynamic multiphase fluid flow using synchrotron-based X-ray microtomography at reservoir conditions. Transp Porous Media 2015;110(1):1–24.
[51] Ohgaki K, Sugahara T, Suzuki M, Jindai H. Phase behavior of xenon hydrate system. Fluid Phase Equilib 2000;175(1):1–6.
[52] Rivers ML. tomoRecon: High-speed tomography reconstruction on workstations using multi-threading. Developments in X-Ray Tomography VIII. 8506. Int Soc Opt Phot 2012::85060U.
[53] FEI. Avizo. 9.7 ed. Hillsboro, OR: FEI; 2018.
[54] Waite WF, Santamarina JC, Cortes DD, Dugan B, Espinoza DN, Germaine J, et al. Physical properties of hydrate-bearing sediments. Rev Geophys 2009;47(4).
[55] Mahabadi N, Dai S, Seol Y, Jang J. Impact of hydrate saturation on water permeability in hydrate-bearing sediments. J Petrol Sci Eng 2019;174:696–703.
[56] Xiao K, Zou C, Lu Z, Deng J. Gas hydrate saturations estimated from pore-and fracture-filling gas hydrate reservoirs in the Qilian Mountain permafrost, China. Sci Rep 2017;7(1):16258.
[57] Tréhu AM, Long PE, Torres ME, Bohrmann G, Rack FR, Collett TS, et al. Three-dimensional distribution of gas hydrate beneath southern Hydrate Ridge: constraints from ODP Leg 204. Earth Planet Sci Lett 2004;222(3):845–62.
[58] Chen X, Verma R, Espinoza DN, Prodanović M. Pore-scale determination of gas relative permeability in hydrate-bearing sediments using X-ray computed micro-tomography and lattice boltzmann method. Water Resour Res 2018;54(1):600–8.
[59] Kneafsey TJ, Seol Y, Gupta A, Tomutsa L. Permeability of Laboratory-Formed Methane-Hydrate-Bearing Sand: Measurements and Observations Using X-Ray Computed Tomography. SPE-139525-PA 2011;16(01):78–94.
[60] Chaouachi M, Neher SH, Falenty A, Kuhs WF. Time resolved coarsening of clathrate crystals: the case of gas hydrates. Cryst Growth Des 2017;17(5):2458–72.
[61] Kuhs WF, Klapproth A, Gotthardt F, Techmer K, Heinrichs T. The formation of meso- and macroporous gas hydrates. Geophys Res Lett 2000;27(18):2929–32.